ASSESSMENT OF FOUR TURBULENCE MODELS IN THE SIMULATION OF A SUPERSONIC NOZZLE AXISYMMETRIC COMPRESSIBLE FLOW

L. DAI[1], A. HADDAD[2]

Turbulent flows Direct Numerical Simulation (DNS) which resolves all turbulent scales is computationally intensive, particularly for high-speed flows like the one investigated herein that deals with supersonic velocities. Turbulence models offer a compromise between computing cost and accuracy, and leads to feasible simulations. This research investigates the use of four models of turbulence in order to simulate the axisymmetric, steady, compressible, supersonic and turbulent expansion of air within a C-D propulsion nozzle designed using the Method of Characteristics (MoC) in 2-D. The results obtained indicate that the k–ω shear-stress transport (SST) model is the most effective choice for accurately predicting the flow characteristics and physical phenomena in such complex turbulent flow environments.

Keywords: C-D Nozzle, Turbulence Models, Method of Characteristics (MoC), CFD simulation, Ansys-Fluent.

1. Introduction

Propulsion nozzles are designed to enhance the velocity of high-pressure fluid by converting the thermal energy of the combustion gases into kinetic energy, thereby producing thrust [1].

Convergent-Divergent (C-D) geometries are used to achieve supersonic velocities making them a critical component in various fields where high-speed flows and efficient thrust generation are needed. They are widely utilized across various engineering applications, especially in the domain of supersonic and hypersonic propulsion [2]. They are furthermore commonly used in diverse wind tunnels where they provide the gas velocity needed for aerodynamic testing [3-4].

The C-D nozzle geometry needs to be accurately represented in the simulation. This includes the wall profile along with its convergence and divergence angles, the throat and exit areas, and other geometrical details that influence the flow. The divergent section is designed using the MoC in 2-D. Initially developed to solve wave equations in physics and engineering [5-6], the MoC gained prominence in the 20th century for its applications in gas dynamics. It

[1] PhD student, LMANM, FST, 8 Mai 1945 university, Algeria, e-mail: lyliadai66@gmail.com
[2] Prof., LMANM, FST, 8 Mai 1945 univ., Algeria, e-mail : haddad.abdelkrim@univ-guelma.dz

has been widely utilized for analyzing supersonic as well as hypersonic flow-fields, playing a crucial role in nozzle design. The core principle of the approach is to transform a system of partial differential equations into a set of total differential equations, which are applied along characteristic paths. These paths represent the directions in which information propagates within the flow-field. In the case of supersonic flows, these characteristic paths align with Mach lines. Nowadays, the MoC, is commonly incorporated into software packages as a numerical method for solving partial differential equations of hyperbolic form, facilitating the design of the propulsion nozzles supersonic sections [7-8].

The simulation of combustion gas expansion in C-D nozzles is conducted using the Reynolds-Averaged Navier-Stokes (RANS) equations, combined with the principles governing mass and energy conservation. They are generally steady-state, which makes them suitable for analyzing nozzle flows [9]. The RANS equations are solved in both the convergent and divergent sections of the nozzle, and are well suited for capturing the turbulent behavior of the flow through modeling the turbulence in a computationally efficient manner.

In the present study, the system of equations integrates the conservation of mass, momentum, and energy equations with turbulent effects. It is solved numerically under the relevant boundary conditions. Various turbulence models are applied to assess their accuracy in estimating the features of turbulent flow-fields in such a complex configuration. The results show that, of the four models considered, the sst k-ω model performed best in simulating supersonic flow-fields within the C-D nozzle.

2. Nozzle sections design

The geometry of the nozzle is illustrated in Figure 1. Similar to that developed earlier [10]; it shows an axisymmetric profile with an ideal truncated contour. The profile is composed by two circular arcs with distinct radii of curvature. That upstream of the throat corresponds to twice the throat radius (R_{tu}=2R_t) while the one downstream is equal to half the throat radius (R_{td}=0.5R_t). At the attachment point labeled 'A' in Figure 1, the downstream arc smoothly transitions into a contour represented by a wall defined by a quadratic polynomial of the second order.

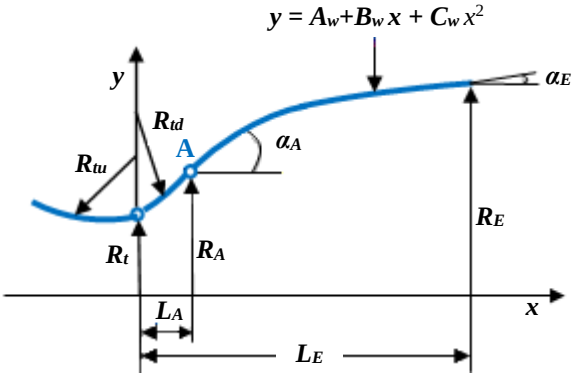

Fig. 1. Nozzle supersonic section profile

The nozzle contour supersonic section has been designed through applying the MoC technique [11-13], and Rao's procedure for the subsonic section [14]. The sonic flow parameters that initiate the Method of Characteristics computations are computed at the throat [15]. All simulations are conducted under cold flow conditions, with an inlet pressure and temperature set at 52bars and 330K, respectively.

2.1 Supersonic nozzle section contour

The MoC approach has been employed to analyze the supersonic flow within the divergent part. This method transforms the differential equations with partial derivatives governing the flow-field into a system of ordinary differential equations (ODEs) that are applied along specific curves. Known as the characteristics, they are represented, in the present case, by the Mach lines. These curves define the pathway for data propagation within the flow domain.

The computations are carried out for an isentropic, inviscid and irrotational flow-field. Such a flow is governed by the equations of continuity (1), that of the momentum (2), the condition of irrotationality (3), and the relation associating the velocity of the flow to the speed of sound (4):

$$\frac{\partial \rho}{\partial t} + v_i \frac{\partial \rho}{\partial x_i} = -\rho \frac{\partial v_i}{\partial x_i} \tag{1}$$

$$\frac{\partial v_i}{\partial t} + v_j \frac{\partial v_i}{\partial x_j} = -\frac{1}{\rho} \frac{\partial p}{\partial x_i} \tag{2}$$

$$\varepsilon_{ij} \frac{\partial v_i}{\partial x_j} = 0 \tag{3}$$

$$a^2 = \partial P / \partial \rho \tag{4}$$

Where (ρ) represents the density of the fluid while (v_i) and (ε_{ij}) illustrate the component of the velocity in the *i*-direction and the Levi-Civita symbol respectively. The pressure is symbolized by (p) and (γ) the ratio of the specific heats. Finally (a) is the speed of sound.

Both thermodynamic and geometric data needed for carrying out the computations using the MoC and therefore defining the nozzle profile supersonic section are shown in Table 1.

Table 1

Input properties for Nozzle MoC computations [10]

Thermodynamic data	Geometrical data
Ambient pressure, $P_a = 0.651\times10^5$ Pa	Throat radius, $R_t = 0.01$ m
Total or stagnation pressure, $P_t = 52\times10^5$ Pa	Throat upstream radius of curvature $R_{tu} = 0.03$ m
Total or stagnation temperature, $T_t = 330$ K	Throat downstream radius of curvature $R_{td} = 0.03$ m
Specific gas constant, $R_G = 280$ J/kg.K	Attachment and Exit angles $\alpha_A = 17.5°$; $\alpha_E = 6.8°$
Specific heat capacity ratio, $\gamma = 1.4$	Exit or divergent section length $L_E = 0.08833$ m

An advantage peculiar to the Method of Characteristics is represented by the fact that as the computations proceeds, the domain mesh and the corresponding profile are produced. The mesh is formed by the left-hand and right-hand characteristics intersection.

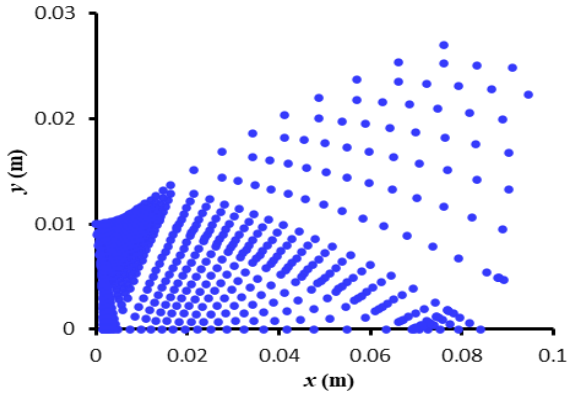

Fig. 2. Computation diagram showing Mach lines

Two kinds of nodes are illustrated: those emanating from the initial-value sonic line determined by Kliegel and Levine approach [15] and those originating from the solid wall whose final profile is generated by the parameters exhibited in Table 2 and which is displayed in Figure 3.

Table 2

Parameters of the configuration generated as a 2nd-degree polynomial wall (MoC)

Computed profile parameters	
Attachment point axial coordinate, L_A	0.00902 m
Attachment point radial coordinate, R_A	0.01139 m
Exit radius, R_E	0.02862 m
2nd-order polynomial wall coefficient (1st), A_w	0.00844
2nd-order polynomial wall coefficient (2nd), B_w	0.33760
2nd-order polynomial wall coefficient (3rd), C_w	-1.23603

2.2 Subsonic nozzle section contour

The main goal of the subsonic section is to increase the flow-field's speed, ensuring it reaches transonic velocities at the throat (the point of minimum area). This enables the flow to achieve supersonic speeds in the nozzle's divergent section. Attached to the upstream circular arc with (R_{tu}) as curvature radius, it forms the entire contour of the nozzle.

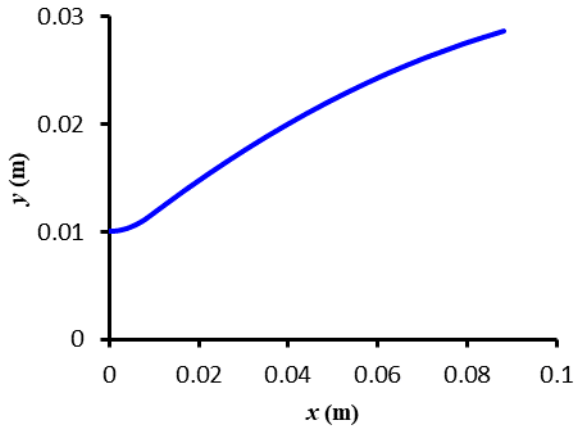

Fig. 3. Divergent section profile

The design of the subsonic section utilizes the Rao technique that has been developed from numerous experimental studies and based essentially on the throat radius [14]. The Rao procedure generates the subsonic profile as:

$$x = 1.5\,R_t\,\cos(\alpha) \qquad \text{and} \qquad y = 1.5\,R_t\,\sin(\alpha) + 2.5\,R_t \tag{5}$$

with:

$$-130° \le \theta \le -90° \tag{6}$$

The layout parameters of the converging section, determined through computations using Rao's technique, are presented in Table 3. The corresponding subsonic configuration is illustrated in Figure 4. When combined with the previously designed divergent contour, it produces the complete C-D de Laval nozzle, as depicted in Figure 1.

Table 3

Converging configuration's factors

θ (°)	x (m)	y (m)
-90	$9.2.\ 10^{-19}$	0.0100
-94	-0.0010	0.0100
-98	-0.0020	0.0101
-102	-0.0031	0.0103
-106	-0.0041	0.0105
-110	-0.0051	0.0109
-114	-0.0061	0.0112
-118	-0.0070	0.0117
-122	-0.0079	0.0122
-126	-0.0088	0.0128
-130	-0.0096	0.0135

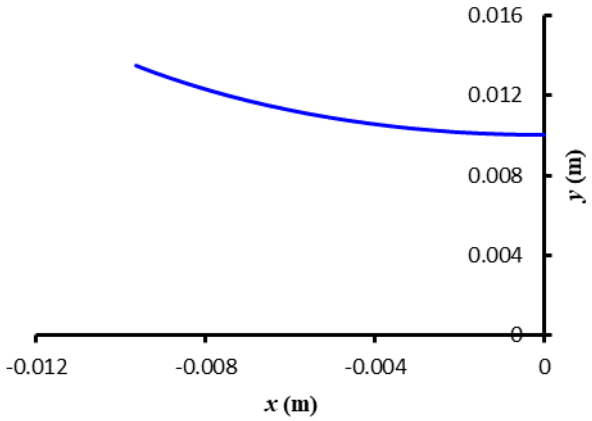

Fig. 4. Nozzle convergent section profile

3. Computational approach and procedure

The computations of such a flow expansion have been performed through applying the Reynolds-Averaged Navier-Stokes (RANS) equations in two

dimensions that have been favored due to their quicker computational turnaround time and their ability to incorporating suitable turbulence models for closure resulting an effective prediction of various complex viscous flows that may be encountered [16]. Flow-field analysis was performed using a two-dimensional model within the finite volume Fluent software [17], incorporating four turbulence closure models that range from nonlinear one- and two-equation models. All simulations were conducted under cold flow conditions.

3.1 Fundamental equations governing the system

The RANS equations along with both the conservation of mass and energy collectively describe the behavior of a steady, compressible, turbulent flow. They may be expressed as:

$$\frac{\partial}{\partial x_i}\left(\rho v_i\right)=0 \tag{7}$$

$$\frac{\partial}{\partial x_j}\left(\rho v_i v_j\right)=-\frac{\partial p}{\partial x_i}+\frac{\partial}{\partial x_j}\left[\mu\left(\frac{\partial v_i}{\partial x_j}+\frac{\partial v_j}{\partial x_i}-\frac{2}{3}\delta_{ij}\frac{\partial v_i}{\partial x_j}\right)\right]+\frac{\partial}{\partial x_j}\left(-\rho\overline{v_i'v_j'}\right) \tag{8}$$

$$\frac{\partial}{\partial t}\left(\rho E\right)+\frac{\partial}{\partial x_i}\left[v_i\left(\rho E+p\right)\right]=-\frac{\partial}{\partial x_j}\left[\left(k+\frac{C_p\mu_t}{0.85}\right)\frac{\partial T}{\partial x_j}\right]+v_i\left(-\rho\overline{v_i'v_j'}\right) \tag{9}$$

Where (v_i') denotes the fluctuations of the velocity in the *i*-direction, and (v_j') those in the *j*-direction. The unknown Reynolds stress tensors are represented by $(\rho\overline{v_i'v_j'})$.

This system is inherently unclosed, necessitating closure of turbulence that requires a modeling of turbulence or Reynolds stress tensors.

3.2 Turbulence models

Four models of turbulence from the eddy viscosity model category are selected and evaluated in the present study. The general Reynolds stress tensor is represented using the Boussinesq assumption and formulated as [18]:

$$-\rho\overline{v_i'v_j'}=\mu_t\left(\frac{\partial v_i}{\partial x_j}+\frac{\partial v_j}{\partial x_i}\right)-\frac{2}{3}\left(\rho k+\mu_t\frac{\partial v_k}{\partial x_k}\right)\delta_{ij} \tag{10}$$

3.2.1 The model of Spalart-Allmaras

The model of turbulence of Spalart-Allmaras [19] is a widely used 1-equation turbulence model. It involves a unique equation of transport for the turbulent kinematic viscosity (v_t), which is derived empirically. It is a robust model with a rapid convergence to a steady state that requires only a degree of mesh refinement near the walls. Originally developed for aerodynamic flows, it is particularly well-suited for aerospace applications engaging wall-bounded flows.

The transport equation governing the modified turbulent viscosity is given as [17]:

$$\frac{\partial}{\partial t}(\rho \nu_t) + \frac{\partial}{\partial x_j}(\rho \nu_t v_i) = G_\nu + \frac{1}{\sigma_{\nu_t}}\left\{\frac{\partial}{\partial x_j}\left[(\mu + \rho \nu_t)\frac{\partial \nu_t}{\partial x_j}\right] + C_{b2\rho}\left(\frac{\partial \nu_t}{\partial x_j}\right)^2\right\} - Y_\nu + S_{\nu_t} \quad (11)$$

Where (G_v) denotes the generation of turbulent viscosity, (Y_v) represents its dissipation in the wall region, caused by the blocking of the wall along with the damping of the viscosity. The constants are represented by (σ_{vt}) and (C_{b2}), while (S_{vt}) denotes a source term specified by the user. In the present case, the last term in Eq. (9) representing the turbulence kinetic energy (k) has been ignored when approximating the Reynolds stresses since it is not computed in the present model.

3.2.2 The conventional k-ε turbulence model

The applied standard k-ε model of turbulence belongs to the 2-equation class, solving two separate transport equations: one for the turbulent kinetic energy (k) and the other for its dissipation rate (ε). Both equations are derived from the transport equations presented below [20]:

$$\frac{\partial}{\partial t}(\rho k) + \frac{\partial}{\partial x_i}(\rho k v_i) = \frac{\partial}{\partial x_j}\left[\left(\mu + \frac{\mu_t}{\sigma_k}\right)\frac{\partial k}{\partial x_j}\right] + G_k + G_b - \rho\varepsilon - Y_M + S_k \quad (12)$$

$$\frac{\partial}{\partial t}(\rho \varepsilon) + \frac{\partial}{\partial x_i}(\rho \varepsilon v_i) = \frac{\partial}{\partial x_j}\left[\left(\mu + \frac{\mu_t}{\sigma_\varepsilon}\right)\frac{\partial \varepsilon}{\partial x_j}\right] + C_{1\varepsilon}\frac{\varepsilon}{k}(G_k + C_{3\varepsilon}G_b) - C_{2\varepsilon}\rho\frac{\varepsilon^2}{k} + S_\varepsilon \quad (13)$$

where (G_b) and (G_k) represent the generation of turbulent kinetic energy, caused by buoyancy effects and mean velocity gradients, respectively. (Y_M) accounts for the impact of compressible turbulence fluctuating dilatation caused by the rate of dissipation. The constants ($C_{3\varepsilon}$), ($C_{2\varepsilon}$) and ($C_{1\varepsilon}$) are predefined

parameters, while (σ_ε) and (σ_k) represent the turbulent numbers of Prandtl for (ε) and (k). The source terms are user-specified and identified as (S_ε) and (S_k).

Since its introduction by Launder and Spalding [21-22], the model of turbulence noted (k-ε) has been widely used in CFD for simulating turbulent flows. Extensively adopted in various industrial applications, it strikes a balance between accuracy and computational cost. It demonstrates considerable robustness and stability across various flow conditions, making it a commonly integrated feature in commercial CFD software packages. It however often requires wall treatment schemes to accurately capture near-wall turbulence behavior in boundary layer flows [23].

3.2.3 The conventional k-ω model of turbulence

The standard model of turbulence (k-ω), originally formulated by Wilcox [24], is a 2-equation model that, unlike the its (k-ε) counterpart, offers improved near-wall predictions by addressing issues related to wall-bounded flows. It solves two distinct transport equations for the turbulent kinetic energy (k) and the turbulent frequency (ω), which represents the specific rate of turbulence dissipation. Both are retrieved from the following relationships [25]:

$$\frac{\partial}{\partial t}(\rho k)+\frac{\partial}{\partial x_i}(\rho k v_i)=\frac{\partial}{\partial x_j}\left(\Gamma_k \frac{\partial k}{\partial x_j}\right)+G_k-Y_k+S_k \tag{14}$$

$$\frac{\partial}{\partial t}(\rho \omega)+\frac{\partial}{\partial x_i}(\rho \omega v_i)=\frac{\partial}{\partial x_j}\left(\Gamma_\omega \frac{\partial \omega}{\partial x_j}\right)+G_\omega-Y_\omega+S_\omega \tag{15}$$

where (G_ω) and (G_k) represent respectively the production of the specific turbulence dissipation rate and that of turbulence kinetic energy from the average gradients of velocity. (Γ_ω) and (Γ_k) serve as the efficient diffusivities for (ω) and (k). The terms (Y_ω) and (Y_k) represent the dissipation of (ω) and (k) caused by turbulence. The source terms are user-specified and identified as (S_ω) and (S_k).

The standard model of turbulence (k-ω) is extensively used in aerospace engineering for simulating aerodynamic flows. It provides improved predictions regions near solid walls as opposed to compared to its (k-ε) counterpart, making it more appropriate for flows involving complex boundary layer interactions.

3.2.4 The k-ω sst model of turbulence

The transport of shear stress (commonly identified as k-ω sst) model is an enhanced version of the basic model (k-ω) described previously, and integrating

supplementary terms to address shear-stress transport outcomes. It combines the (k-ω) model of Wilcox [24] and that of Launder-Sharma [26] by using an adjustment function in the (ω) equation. This hybrid approach leverages the strengths of both models, offering improved accuracy in predicting turbulent flows in both free-stream areas and the regions near the walls. By combining features from both the standard models (k-ε) and (k-ω), it enhances predictions near the walls [27]. The resulting model is expressed as:

$$\frac{\partial}{\partial t}(\rho k)+\frac{\partial}{\partial x_i}(\rho k v_i)=\frac{\partial}{\partial x_j}\left(\Gamma_k \frac{\partial k}{\partial x_j}\right)+G_k-Y_k+S_k \tag{16}$$

$$\frac{\partial}{\partial t}(\rho \omega)+\frac{\partial}{\partial x_i}(\rho \omega v_i)=\frac{\partial}{\partial x_j}\left(\Gamma_\omega \frac{\partial \omega}{\partial x_j}\right)+G_\omega-Y_\omega+D_\omega+S_\omega \tag{17}$$

where all parameters are defined similarly to those in the standard model (k-ω) described in the previous section, except for (D_ω), which represents the cross-diffusion component [17].

The k-ω sst model of turbulence offers improved near-wall predictions and accuracy compared to its standard (k-ω) counterpart, particularly in flows with complex boundary layer interactions and adverse pressure gradients. This increased robustness, however, results in higher computational costs. Several investigations have evaluated the predictive capabilities of turbulence models across diverse flow configurations. Studies have focused on turbulent plane jets [28], corrugated pipes with complex heat transfer and separation [29], and transonic aerodynamics, where Spalart–Allmaras and k–ω SST showed superior performance in capturing shocks and boundary-layer interactions [30].

3.3 Domain discretization and mesh generation.

The selection of the spatial mesh in the 2-D computational domain impacts the resulting solution. A finer grid results in minor variations in the fundamental structure of the flow-field but raises computational expenses. Therefore, the selected mesh should strike a balance between precision and computational efficiency.

A mesh adjustment investigation analysis was carried out in order to examine the predicted pressure distribution along the centerline and wall (Figure 5) using three different meshes. The results for a rough (50 x 12), fine (145 x 30), and dense (200 x 64) grids align with an overall numerical cell counts of 600, 4,350, and 12,800 within the nozzle, respectively. At the onset of subsonic expansion (Figure 5-a) and near attachment point i.e. around $x/R_t = 1$ (Figure 5-b), the comparison reveals that the results obtained from the (145 × 30) and (200 ×

64) meshes in the C-D nozzle are highly similar. Consequently, the (145 × 30) grid is chosen to optimize computational efficiency. In this configuration, grid is refined near the wall with a non-dimensional wall distance (Y+) set to unity and thirty points distributed within the wall boundary layer, as illustrated in Figure 6.

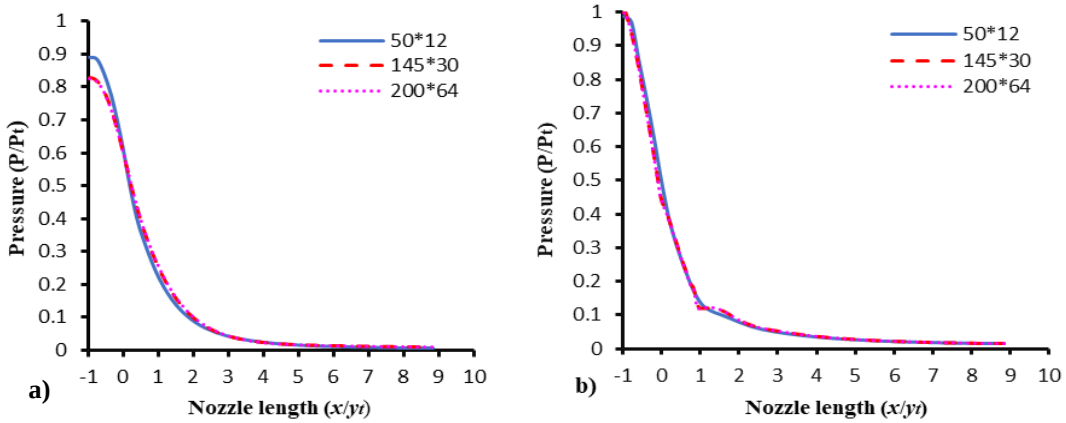

Fig. 5. Distributions of dimensionless pressures using rough, fine and dense grids along a) centerline and b) wall

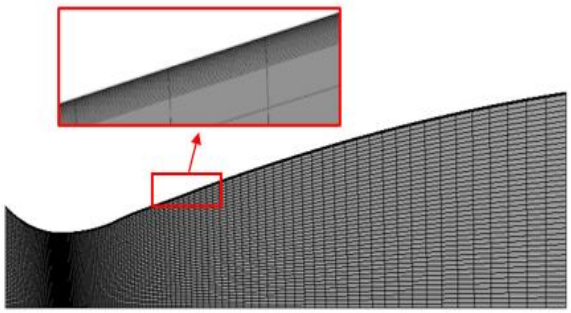

Fig. 6. Nozzle grid topology

Figure 7 illustrates the computational domain, the boundary conditions being outlined in Table 4, which summarizes key settings used to simulate the expansion within the C-D nozzle.

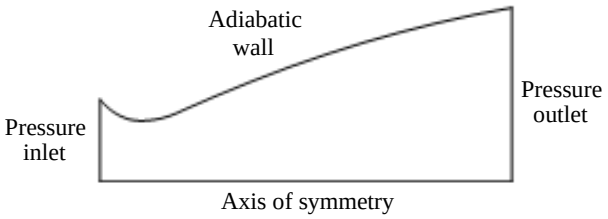

Fig. 7. Boundary conditions

Table 4

Main simulation settings

Features applied	
Approach	Density related
Feature	Perfect gas
model of viscosity	Inviscid, Spalart-Allmaras, *k-ε*, *k-ω*, sst *k-ω*
Operational pressure	0.
Inlet boundary conditions	P_t =52×10^5 Pa ; T_t =330 K
Outlet boundary conditions	P_a =0.651×10^5 Pa
Residuals	10^{-6}

4. Results and discussion

Figure 8 displays the temperature, pressure, and Mach number contours for the five cases examined for the four turbulence models presented earlier. The general flow structure appears consistent across the cases, with a visible boundary layer in the viscous flow scenarios, particularly evident in the Mach and temperature contours. This boundary layer progressively thickens from the nozzle inlet to the outlet. Importantly, no instances of flow separation were observed in these cases.

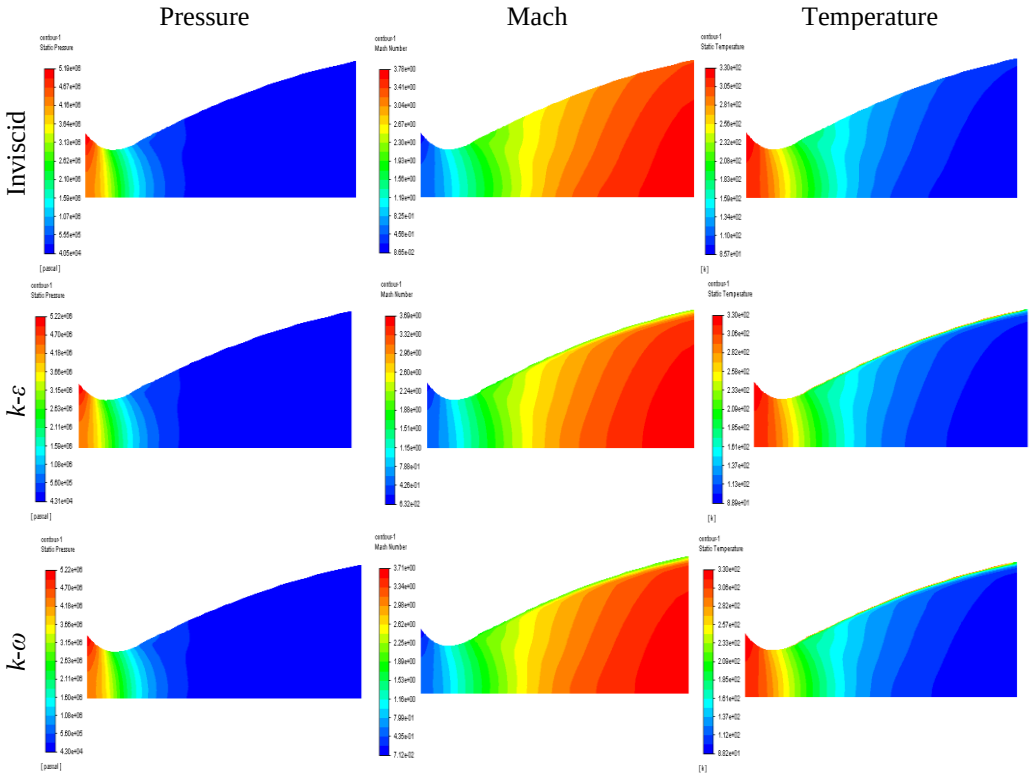

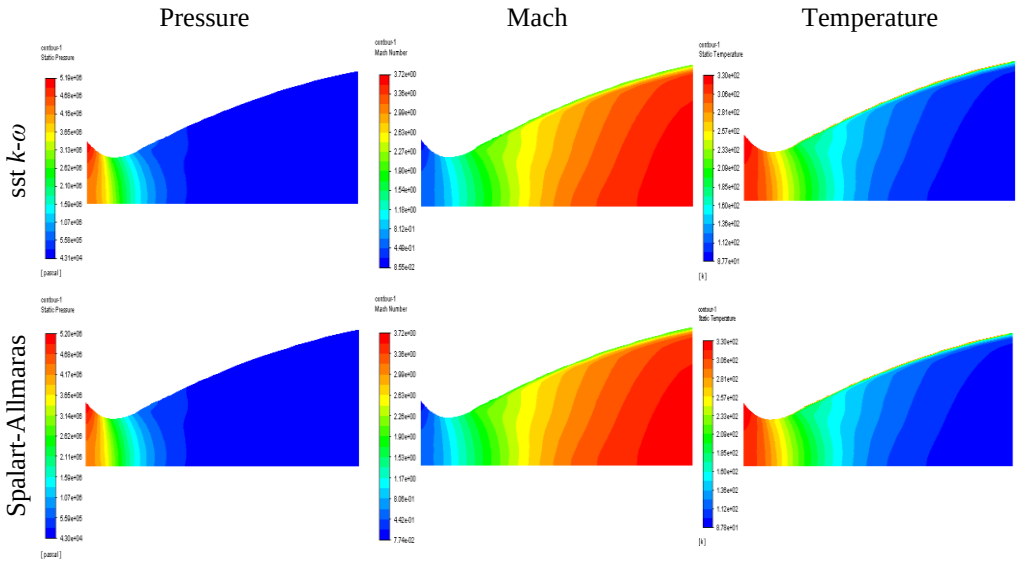

Fig. 8. Pressure, Mach number, and Temperature contours for the five cases examined

Figure 9 presents a comparison of the computational outcomes derived from the four models of turbulence. The static pressure and static temperature are normalized by the total pressure (P_t) and total temperature (T_t), respectively. The pressure, temperature, and Mach number are plotted as functions of the normalized streamwise position (x/R_t). The evolution seems to follow a similar trend across the four models, yielding very close results. The MoC profile exhibits a distinct feature for both pressure and temperature profiles along the centerline. This point of discontinuity, denoted as 'A' and identified as the attachment point in Figure 1, plays a critical role in illustrating the fundamental behavior of the expanding supersonic flow. It illustrates the location where the initially separated characteristics converge and reattach, thereby delineating a distinct change in the flow regime. The MoC captures this phenomenon with high fidelity, as its computational framework is based on the propagation of information along Mach lines. Consequently, it not only resolves the local discontinuity with accuracy but also provides deeper insight into the supersonic global expansion process.

The flow-field is described by the fundamental equations that express the conservation of mass, momentum, and energy. To evaluate the convergence of the iterative solution, the scaled residual is used. This metric is commonly employed as a reliable indicator in most CFD simulations. As presented in Table 4, a threshold of (10^{-6}) has been selected, ensuring a strict convergence benchmark.

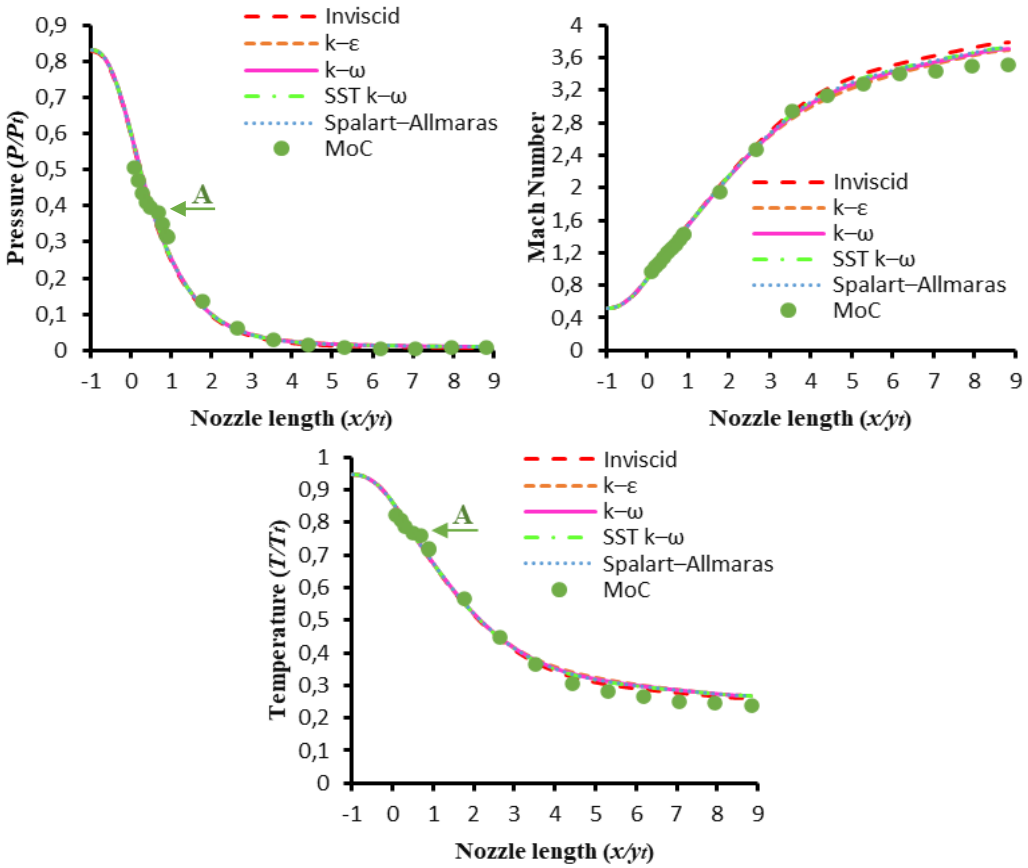

Fig. 9. Comparison of the centerline pressure ratios, Mach and temperature ratios

Figure 10 depicts the number of iterations required to achieve computational convergence for the four cases examined. It demonstrates a rapid convergence of the sst k-ω, reached in 1,764 iterations (Figure 10-a). In contrast, the k-ε (Figure 10b) required over 3,000 iterations to reach similar results. The Spalart-Allmaras achieved convergence in 2,223 iterations (Figure 10c), whereas the k-ω model was comparatively slower, requiring 2,483 iterations (Figure 10d). This suggests that k-ω was less efficient in terms of convergence speed compared to the other three models. Spalart-Allmaras, with its relatively faster convergence, presents an appealing alternative to both k-ε and k-ω approaches.

In this particular case, the underlying reason behind the sst k-ω efficiency may be attributed to its transitional approach that combines the strengths of k–ε and k–ω, switching between them depending on the flow region, and is therefore better suited to shock–boundary layer interactions and complex nozzle flows. The Spalart–Allmaras model, while efficient and robust for attached aerodynamic flows, tends to lose accuracy in cases involving strong separation or complex shock–boundary layer interactions. The standard k–ε model is widely applied for

engineering flows but is known to perform poorly in near-wall regions and in predicting adverse pressure gradient effects. The conventional *k–ω* model captures near-wall behavior more reliably; however, it is overly sensitive to free-stream conditions, which can compromise accuracy in external aerodynamic applications.

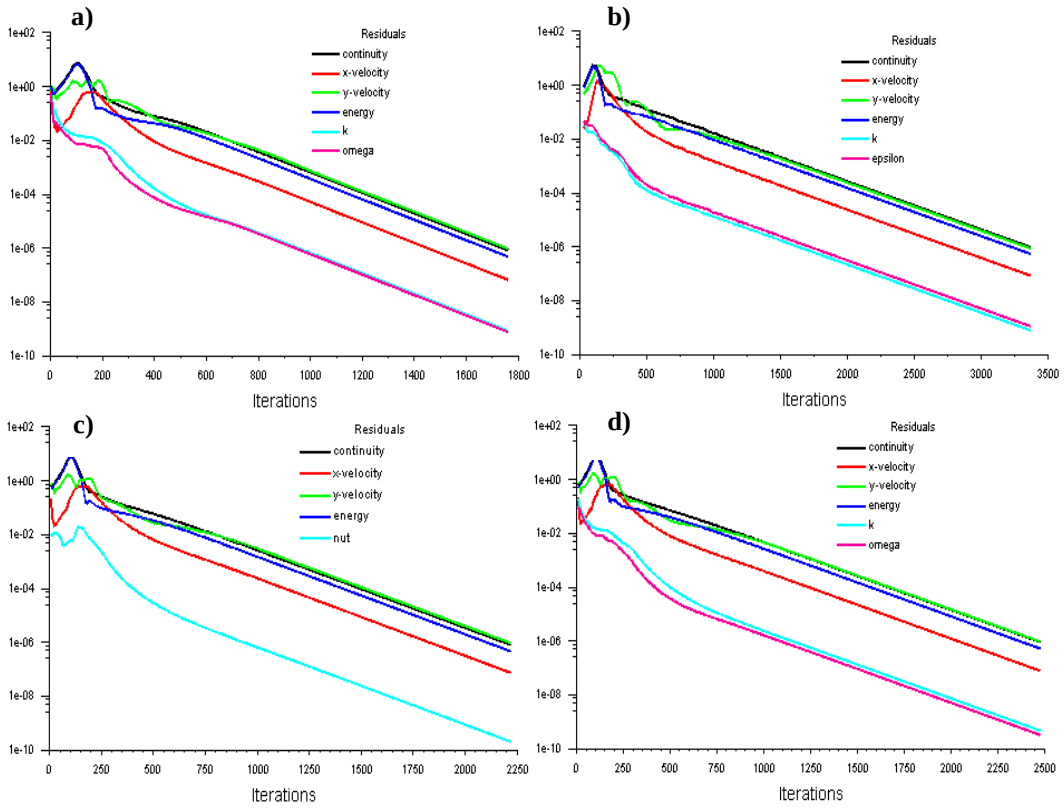

Fig. 10. Flow-field calculations scaled residuals
a) sst *k-ω*, b) *k-ε*, c) Spalart-Allmaras, d) *k-ω*

5. Conclusions

Four turbulence models were assessed to determine their effectiveness in achieving accuracy and rapid convergence for predicting pressure, Mach number, and temperature distributions along a convergent-divergent propulsion nozzle operating at a nozzle pressure ratio (NPR) of 80. The results obtained reveal that, among the four models tested, the RANS equations combined with the sst *k-ω* closure model proved to be the most effective for solving such supersonic internal flow problems. It demonstrated superior performance in both computational

efficiency (computational time) and accuracy. This efficacy is largely attributed to its ability to leverage the strengths of the k-ε and k-ω models, enabling accurate and reliable predictions across a broad spectrum of turbulent flows. As a result, the sst k-ω model is a dependable choice for a vast array of complex turbulent flow scenarios.

The Spalart-Allmaras model demonstrated relatively rapid convergence. Even though a one-equation transport model, it demonstrated relatively rapid convergence with a notable accuracy compared to its counterparts. It focuses on predicting the turbulent kinematic viscosity transport, which effectively models turbulence across the flow-field. This simplification in computation makes it particularly well-suited for aerospace engineering applications, such as internal aerodynamic flows.

In contrast, both k-ε and k-ω struggled for converging compared to their two precedent counterparts. Even though the (k-ω) model does not need any wall function to directly resolve the near-wall region, it seems to be nevertheless sensitive the free-stream values of (ω) that may lead it to inaccuracies in regions away from walls. On the other hand, k-ε relies on wall functions for near-wall treatment but performs well in free-stream regions. However, for the current case involving complex boundary layer flows, the k-ω sst model is the most suitable option. For simpler and faster computations, the Spalart-Allmaras model provides an excellent alternative.

The insights gained from these turbulence model evaluations extend beyond the specific cases studied and can inform simulations of other nozzle geometries, compressibility regimes, and even high-enthalpy flows. While model performance may vary with flow complexity, the comparative trends, such as the robustness of k–ω sst in shock-boundary layer interactions or the efficiency of Spalart–Allmaras in attached flows, provide valuable guidance for selecting appropriate closures in diverse applications. Such generalization is particularly relevant for aerospace propulsion systems, where accurate prediction of separation, heat transfer, and shock behavior is critical to design and performance optimization.

Acknowledgement

This research was conducted at ‘université 8 Mai 1945’, Guelma, Algeria, as part of the PRFU research A11N01UN240120210001. The authors extend their gratitude to the ‘General Directorate for Scientific Research and Technological Development’ for their valuable support and contributions to this work.

R E F E R E N C E S

[1]. *J. Bahamon, M. Martinez*, "Study of fluid-dynamic behavior in a convergent–divergent nozzle by shape optimization using evolutionary strategies algorithms", Proceedings of the Institution of Mechanical Engineers, Part G: Journal of Aerospace Engineering, 237(12), 2023, pp. 2844-2862. https://doi.org/10.1177/09544100231163372

[2]. *S. Khare, U.K. Saha*, "Rocket nozzles: 75 years of research and development", Sādhanā, 46(2), 76, 2021. https://doi.org/10.1007/s12046-021-01584-6

[3]. *A. Arshad, S. Samarasinghe, and V. Kovalcuks*, "A simplified design approach for high-speed wind tunnels. Part-II: Optimized design of settling chamber and inlet nozzle", In 2020 11th International Conf. on Mech. & Aerospace Eng., ICMAE, 2020, pp. 150-154. https://doi.org/10.1109/ICMAE50897.2020.9178865

[4]. *S. Zahir, U.B. Aamer, A.U. Haque, and K.R. Qureshi*, "Wind tunnel's supersonic CD nozzle design and flow analysis", In 17th Asian Congress of Fluid Mechanics, ACFM-2023, vol. 2023, pp. 295-299. https://doi.org/10.1049/icp.2023.1964

[5]. *A.L. Cauchy*, "Mémoire sur les systèmes d'éq. aux dérivées partielles d'ordres quelconques, et sur leur réduction à des systèmes d'équations linéaires du premier ordre", 1842.

[6]. *S.V. Kowalevsky*, Zur Theorie der partiellen Differentialgleichung, 1875. https://doi.org/10.1515/crll.1875.80.1

[7]. *S. A Hashim, S. Dharmalingam*, "Design of smooth supersonic nozzle profile using method of characteristics", In *AIP* Conference Proceedings, AIP Publishing vol. 2821, no. 1, 2023. https://doi.org/10.1063/5.0164552

[8]. *Y. Wang, and Z. Jiang*, "Theories and methods for designing hypersonic high-enthalpy flow nozzles", Chin. J. Aeronaut., 35, 2022, pp. 318-339. https://doi.org/10.1016/j.cja.2021.01.018

[9]. *K. Bhide, S. Abdallah*, "High-Order Accurate Numerical Simulation of Supersonic Flow Using RANS and LES Guided by Turbulence Anisotropy", 2022, Fluids, 7(12), 385. https://doi.org/10.3390/fluids7120385

[10]. *P. Reijasse, D. Coponet, J.M. Luyssen, V. Bar, S. Palerm, J. Oswald, and P. Kuszla*, "Wall pressure and thrust of a dual bell nozzle in a cold gas facility", Progress in Propulsion Physics, 2, 2011, pp. 655-674. https://doi.org/10.1051/eucass/201102655

[11]. *M.J. Zucrow, J.D. Hoffman*, "Gas dynamics. Vol. 2-multidimensional flow", 1977.

[12]. *J.G. Allman, J.D., Hoffman*, "Design of maximum thrust nozzle contours by direct optimization methods". AIAA journal, 19(6), 1981, pp. 750-751. https://doi.org/10.2514/3.50999

[13]. *T. Fernandes, A. Souza, and F. Afonso*, "A shape design optimization methodology based on the method of characteristics for rocket nozzles". CEAS Space Journal, 15(6), 2023, pp. 867-879. https://doi.org/10.1007/s12567-023-00511-1

[14]. *D.Y.K. Uyeki*, "A design method for a supersonic axisymmetric nozzle for use in wind tunnel facilities". MSc in Aerospace Engg, Dept of Aerospace Engg, Dan José University, 2018.

[15]. *J.R. Kliegel, J.N. Levine*, "Transonic flow in small throat radius of curvature nozzles", *AIAA Journal*, *7*(7), 1969, pp. 1375-1378. https://doi.org/10.2514/3.5355

[16]. *F.G. Schmitt*, "About Boussinesq's turbulent viscosity hypothesis: historical remarks and a direct evaluation of its validity". Comptes Rendus Mécanique, 335(9-10), 2007, pp. 617-627. https://doi.org/10.1016/j.crme.2007.08.004

[17]. *** ANSYS inc.- Ansys Fluent Theory Guide, Release 2022R1, 2022.

[18]. *J.O. Hinze*, "Turbulence", McGraw, 1975.

[19]. *P. Spalart, S. Allmaras*, "A one-equation turbulence model for aerodynamic flows", In 30th Aerospace Sc. Meeting and exhibit, 1992. https://doi.org/10.2514/6.1992-439

[20]. *T.H. Shih, W.W. Liou, A. Shabbir, Z. Yang, and J. Zhu*, "A new *k-ϵ* eddy viscosity model for high Reynolds number turbulent flows", Computers & fluids, 24(3), 1995, pp. 227-238. https://doi.org/10.1016/0045-7930(94)00032-T

[21]. *B.E. Launder, D.B. Spalding*, "Lectures in mathematical models of turbulence", (No Title), 1972.

[22]. *B.E. Launder, D.B. Spalding*, "The numerical computation of turbulent flows", In Numerical prediction of flow, heat transfer, turbulence and combustion, 1983, pp. 96-116, Pergamon. https://doi.org/10.1016/B978-0-08-030937-8.50016-7

[23]. *V. Yakhot, S.A. Orszag*, "Renormalization group analysis of turbulence. I. Basic theory", Journal of scientific computing, 1(1), 1986, pp. 3-51. https://doi.org/10.1007/BF01061452

[24]. *D.C. Wilcox*, "Turbulence modeling for CFD", La Canada, CA: DCW industries, vol. 2, 1998, pp. 103-217.

[25]. *F.R. Menter*, "Review of the shear-stress transport turbulence model experience from an industrial perspective", Int. J. of Computational Fluid Dynamics, 23(4), 2009, pp. 305-316. https://doi.org/10.1080/10618560902773387

[26]. *B.E. Launder, B.I. Sharma*, "Application of the energy-dissipation model of turbulence to the calculation of flow near a spinning disc", Letters in heat and mass transfer, 1(2), 1974, pp. 131-137

[27]. F.R. Menter, "Two-equation eddy-viscosity turbulence models for engineering applications", AIAA journal, 32(8), 1994, pp. 1598-1605. https://doi.org/10.2514/3.12149

[28]. *S. Ziou, J. Xiao*,and *X.D. Chen*, "A comprehensive comparison of different Reynolds-averaged Navier-Stokes turbulence models in modeling turbulent plane jets", ACSOmega, 10, 2024, pp. 19873-19886. http://pubs.acs.org/journal/acsodf

[29]. *T.T. Tang, F.Q. Li, G.Y. Wang, J. Yan, and Z.K. Lu*, "Comparative Study of RANS Models for Simulating Turbulent Flow and Heat Transfer in Corrugated Pipes", Water, 17 (17), 2025, https://doi.org/10.3390/w17172649

[30]. *M.H.M. Mazumder*, "Comparative study of turbulence models in CFD for transonic flow over the ONERA M6 wing", Discov Mechanical Engineering 3, 46, 2024, https://doi.org/10.1007/s44245-024-00080-5